City, University of London Institutional Repository

Hysteretic Behavior and Multi-Wave Buckling of Assembled Buckling-Restrained Braces Wrapped with Fiber Clothes

Jinzhou He[*], Mingming Jia[*,†,‡,||], Shan Gao[*,§], Wufeng Li[*],
Dagang Lu[*,†,‡] and Feng Fu[¶]

[*]*School of Civil Engineering*
Harbin Institute of Technology
Harbin 150090, P. R. China

[†]*Key Lab of Structural Dynamic Behavior*
and Control of the Ministry of Education
Harbin Institute of Technology
Harbin 150090, P. R. China

[‡]*Key Lab of Smart Prevention and Mitigation*
of Civil Engineering Disasters of the Ministry of Industry
and Information Technology
Harbin Institute of Technology
Harbin 150090, P. R. China

[§]*Postdoctoral Station of Civil Engineering, Chongqing University*
Chongqing 400000, P. R. China

[¶]
School of Mathematics, Computer Science and Engineering
City, University of London, London, UK
[||]*jiamingming@hit.edu.cn*

To rapidly repair the damaged buckling-restrained brace serving as energy absorption member during earthquake, the assembled method of wrapping the component with FRP cloth is pro-posed. In this research, a series of cyclic tests on six assembled buckling-restrained brace (ABRB) wrapped with three kinds of FRPs (carbon fiber, glass fiber and basalt fiber) were performed. The tested results show that all the specimens show excellent hysteretic performance and similar damage mode, namely core unit fracture, whilst short specimens show better duc-tility, but worse energy dissipation ability than the long specimen. A parametric analysis is performed based on a finite element model validated against the test result. The effects of the gap and friction force between core unit and infilled concrete and the thickness of FRP cloth are analyzed. The modes of multi-wave buckling of core units are exhibited, and the influence of multi-wave buckling on component performance is evaluated. Based on the test and simulation analysis, CFRP is suggested to be used in the wrapped buckling-restrained brace.

Keywords: Assembled buckling-restrained brace; ⁻ber reinforced polymer; hysteretic behavior; multi-wave buckling; energy dissipation capacity.

[||]Corresponding author.

1. Introduction

Compared with ordinary steel brace, besides excellent energy dissipation capacity, buckling-restrained braces (BRBs) can withstand large compressive forces without buckling. Many studies have been performed on the energy dissipation and stability of different types of BRBs through experimental, numerical and theoretical analysis to guide engineering application. Normally, the traditional BRBs adopt a monolithic type, that is, the core unit and the restraint unit are integrally assembled, such as concrete filled steel tube. In 1973, Wakabayashi et al.[1] proposed the concept of BRB by embedding a steel plate in the concrete slab which showed good seismic performance. Nakamura et al.[2] proposed a formula for calculating the fatigue life of the BRB considering the strain concentration. Merritt et al.[3] conducted a test of six BRBs' subsystems and studied the influence of the BRBs' end rotation on the support performance. Deng[4] used four GFRP tubes as the constraint elements of the BRB core unit. The failure modes mainly include local buckling, multi-wave buckling and core fracture.

However, the costs for repairing or replacing conventional BRB after damage in an earthquake are often high. Therefore in recent years, there has been an increasing interest in assembled buckling-restrained braces (ABRBs). Iwata et al.[5] conducted experimental studies on steel-concrete assembled BRBs. The design method was proposed based on the failure mode of the tested specimens. Ali Gheidi et al.[6] studied the effect of filler materials on the overall buckling resistance and local stability. The test results showed that the concrete of 25 MPa and 30 MPa can effectively prevent the overall and local stability of the BRB. Chou et al.[7] proposed an ABRB by using steel plates as core units, and steel plates and bolts as restraint units, which showed good energy dissipation performance and resilience. Takeuchi et al.[8] considered the influence of local buckling of core elements on BRB performance and proposed a design method to prevent local buckling. Emrah[9] studied the buckling constraint mechanism of welded and bolted rolling of BRBs and discussed the effect of the bolt pre-stress in the support on the BRB performance. Eryasar et al.[10] discussed conducted the effects of bolt number, slenderness ratio, width-thickness ratio and geometric defects on the hysteretic behavior of BRB. Hoveidae et al.[11] concluded by simulation that the bending stiffness can significantly affect the overall stability of BRB. Gennaa[12] analyzed the relationship between the axial force and the multimode buckling deformation wavelength of the inner core. Perter Dusicka et al.[13] used the FPR tube as the restraint unit and the steel as the core unit to assemble BRB, which solved the self-weight influence of the BRB during installation. Wang et al.[14,15] proposed the aluminum alloy BRB and studied its low cycle fatigue performance and plastic damage development through experiments. The strain-based damage assessment formula was given in the research. Miller et al.[16] used a new type of

N-T memory alloy as the core unit of BRB which showed better hysteretic behavior. Jia[17,18] studied the stability, ductility and hysteretic behavior of the BRB of the I-shaped non-yield segment. The study showed that the stability of the joint segment would directly affect the ductility of the component.

In this paper, the specimens of ABRB wrapped with fiber reinforced polymer (FRP) cloth were designed, aiming to study the rapid repair technologies for BRBs damaged during earthquake. The corrosion resistance of outer fiber material is also better than outer steel tube. To this end, three groups of circular ABRBs wrapped with FRP, namely carbon fiber, glass fiber and basalt fiber, respectively, were tested. A parametric analysis is performed based on a finite element model validated against the test result. The hysteretic behavior of assembled BRBs wrapped with fiber clothes was researched and the multi-wave buckling of components was discussed especially.

2. Specimens' Preparation

In the test, six specimens were designed and denoted by length and type of outer fiber: L/S means long/short type of FRP cloth, respectively, whilst B/G/C means basalt/glass/carbon fiber cloth, respectively, as shown in Fig. 1. For example, L-B means the ABRB wrapped with long type basalt fiber cloth. The appearances of three fibers are shown in Fig. 1, which are helpful to know the properties of different fiber materials.

As shown in Fig. 2, based on the length of ABRB core unit (1 200 mm and 1 500 mm), the length of the constrained yielding section is 720 mm and 900 mm, respectively, the lengths of the constrained non-yield segments are 240 mm and 300 mm, respectively, and the lengths of the unconstrained non-yield segments are 240 mm and 300 mm, respectively. The restrained yielding section of the ABRB core unit is 8-mm-thickness steel plate with a section width of 80 mm and 100 mm, respectively.

The schematic diagram of ABRB is shown in Fig. 2(d), and the new ABRB is composed of three components, i.e. the core plate element, a pair of concrete infilled channel steel, and the wrapped carbon or basalt fiber cloth.
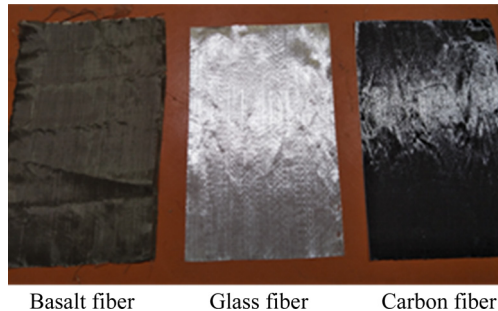
Basalt fiber   Glass fiber   Carbon fiber

Fig. 1. Three kinds of fiber clothes.

i) Planar graph

ii) cross-section view

iii) Side elevation graph

(a) Short ABRB core unit

i) Planar graph

ii) cross-section view

iii) Side elevation graph

(b) Long ABRB core unit

i) Long specimen

ii) Short specimen
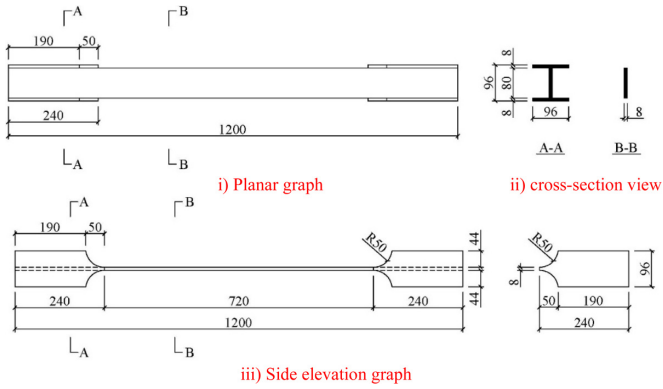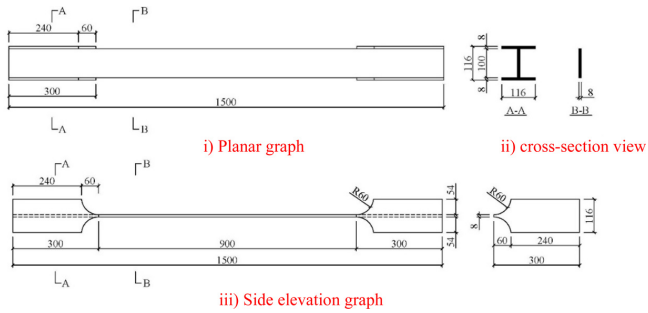
(c) Cross-section of ABRBs
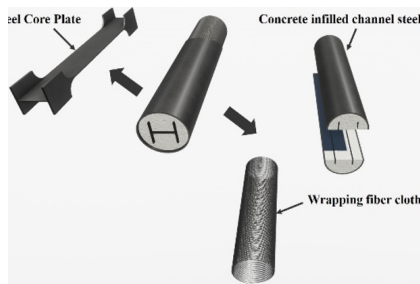
(d) Schematic diagram of ABRB

Fig. 2. Three kinds of fiber clothes.

i) Sealing plate

ii) Half-round steel plate with sealing plate

(a) Fabrication of half-round steel plate

i) Wooden mold

ii) Half-round steel plate casted with concrete

(b) Fabrication of constrain member

i) Installing core unit

ii) Fix two halves by spot welding

iii) Wrapping FRP

(c) Fabrication of constrain members and core unit

Fig. 3. Fabrication of ABRB specimen.

The fabrication of the ABRB specimens follows the specific procedure as follows:

(1) Rolling two half round 4-mm-thickness steel plates which can be assembled together as a 219-mm-diameter tube; welding two 10-mm-thickness drilled sealing plates at the ends of the half-round steel plate, as shown in Fig. 3(a).

(2) Making two wooden molds which is identical to the half of core unit; casting concrete into two half-round steel plates separately and putting the wooden mold into the concrete to make a position for core unit, as shown in Fig. 3(b)

(3) After healing the concrete for some time, removing the wooden mold and installing core unit into one half-round steel plate casted with concrete, namely constraint member; assembling the other half and fixing two halves with spot welding; wrapping the two halves of constraint members and core unit with FRP cloth, as shown in Fig. 3(c).

It should be mentioned particularly that the outer tube consisting of two half-round steel plates did not have a continuous section, namely unable to sustain loop force to confine the infilled concrete and core unit. Even though they indeed contributed to the stiffness of the specimen, this assembled tube only served as a mold for concrete casting. The infilled concrete was only confined by FRP cloth.

Table 1. Specimen design parameter.

Specimen	Core cross section (mm)	Yield length (mm)	Inner steel plate	Channel steel strength	Concrete strength	Outer fiber
S-B	80 × 8	720	Q235B	Q235B	C40	B
S-G	80 × 8	720	Q235B	Q235B	C40	G
S-C	80 × 8	720	Q235B	Q235B	C40	C
L-B	100 × 8	900	Q235B	Q235B	C40	B
L-G	100 × 8	900	Q235B	Q235B	C40	G
L-C	100 × 8	900	Q235B	Q235B	C40	C

Fig. 4. Core unit covered with unbounded materials.

To ensure that the friction between the core steel unit and the in-filled concrete is as small as possible, and the in-filled concrete only provides constraints on the core unit, and not directly bear the axial force, as shown in Fig. 4, the unbonded material of 2-layer polyvinyl chloride plastic film was used to cover the core unit.

3. Material Test

3.1. *Steel*

The ABRB core unit and the outer tube are all made of Q235B steel for which steel coupons were designed as shown in Fig. 5. In order to measure the actual yield strength of steel accurately, the tensile loading was applied at the rate of 0.5 mm/s. The elastic modulus and Poisson's ratio were measured by using the horizontal and longitudinal strain gauges placed on the coupons. The mechanical properties of the steel were tested as shown in Fig. 6 and Table 2.
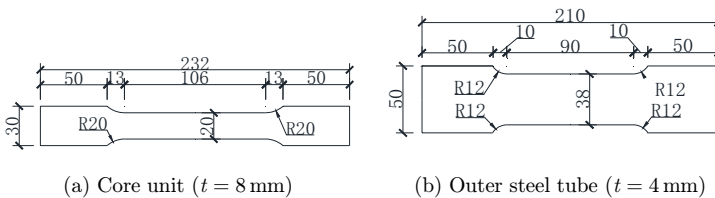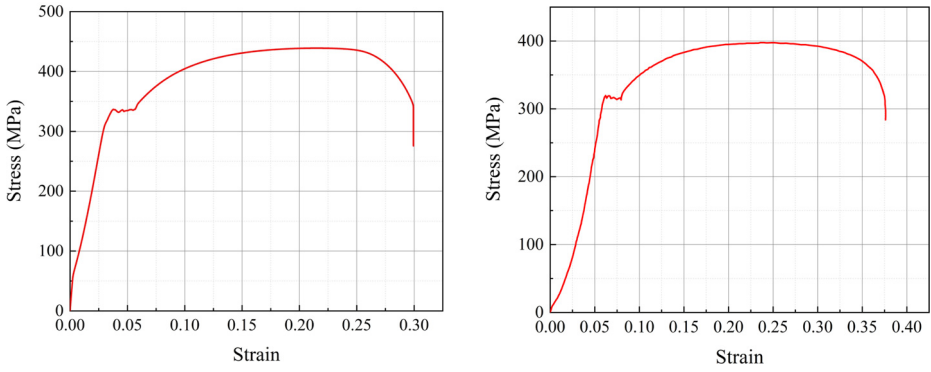

(a) Core unit ($t = 8$ mm)   (b) Outer steel tube ($t = 4$ mm)

Fig. 5. Steel coupon design.

(a) The stress-strain curve of the inner core steel   (b) The stress-strain curve of the outer tube steel

Fig. 6. Stress–strain curves of the tested steel.

Table 2. Steel mechanical properties.

	f_y (MPa)	f_u (MPa)	f_u/f_y	E_s ($\times 10^5$ MPa)	ν Poisson's ratio
Core unit	341	446	1.304	2.06	0.307
Outer tube	322	408	1.267	2.01	0.285

Table 3. Concrete mechanical properties.

| f_c MPa	E_c GPa	Poisson's ratio v
29.3	30.3	0.235

3.2. *Concrete*

Since the space for casting concrete was limited, fine stone concrete was used to ensure smooth pouring and smooth concrete flow. The maximum particle size of coarse aggregate should be strictly controlled under 5 mm. The tested mechanical properties of concrete are listed in Table 3.

3.3. *FRP*

In order to test the basic mechanical properties of FRP, including longitudinal tensile, horizontal tensile, longitudinal compression, transverse compression and longitudinal and transverse shear behavior, the coupons were prepared according to relevant Chinese standards, as shown in Fig. 7. The design parameters of detailed dimensions of FRP coupons are listed in Table 4. The longitudinal and horizontal strains of the coupon were measured by strain gauges to calculate the elastic modulus, Poisson's ratio and shear modulus of FRP in both directions.

The tested specimens are shown in Fig. 8. The tensile test specimen was fractured at the middle or the end whilst the fiber was torn and the fracture section was
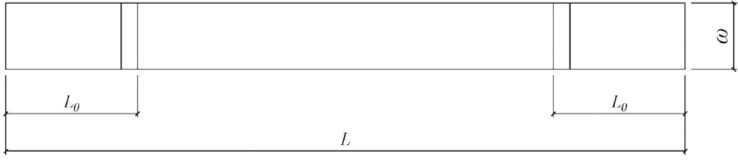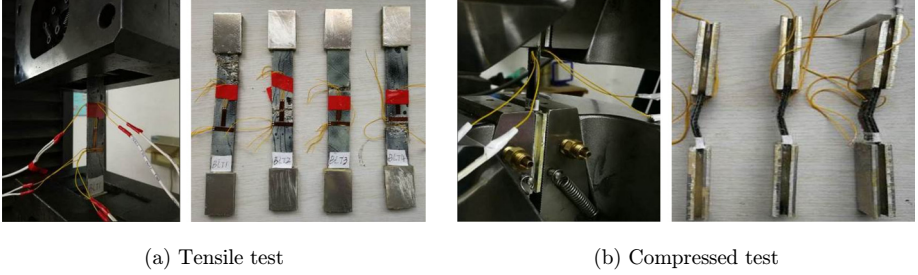
(a) Planar graph

(b) Side elevation graph

Fig. 7. FRP coupon design.

(a) Tensile test

(b) Compressed test

Fig. 8. Material tests of FRPs.

uneven. The compressive test specimen was generally broken in the middle whilst the fracture section was relatively flat. The damage of the specimens was mainly resultant of the buckling. Due to the initial defects of the specimens, out-of-plane deformation would inevitably occur in the compressive test.

From the mechanical properties' test results, it is concluded that the mechanical properties of basalt fiber are worse than those of carbon fiber and glass fiber. The carbon FRP, glass FRP and blast FRP are brittle materials, and the mechanical properties of the FRP materials are shown in Table 5, where f_{tL}, f_{cL}, f_{tH}, f_{cH}, f_s, G_s, E_L, E_H and v represent the ultimate longitudinal tensile strength, ultimate longitudinal compressive strength, ultimate transverse tensile strength, ultimate transverse compressive strength, ultimate shear strength, shear modulus, longitudinal elastic modulus, transverse elastic modulus and Poisson's ratio, respectively.

Table 4. Design parameters of FRP coupons.

Test	L (mm)	L_0 (mm)	w (mm)	h (mm)	δ (mm)
Tensile specimen	250	50	25	3	3
Compressive specimen	140	50	10	3	3
Shear specimen	250	50	25	3	3

Table 5. Mechanical properties of FRP.

Specimens	f_{tL} (MPa)	f_{cL} (MPa)	f_{tH} (MPa)	f_{cH} (MPa)	f_s (MPa)	G_s (GPa)	E_L (GPa)	E_H (GPa)	v
CFRP	725.02	138.77	23.56	41.95	27.60	1.71	15.44	2.62	0.34
GFRP	250.13	130.89	3.93	40.32	22.80	1.51	7.21	1.47	0.44
BFRP	94.27	62.77	94.27	62.77	19.60	1.16	6.27	3.96	0.18

4. Test Setup and Procedure

The post-yield loading protocols are listed in Table 6.

The loading in the test was divided into two phases, the elastic phase and the post-yield phase. In the elastic phase, the specimen was pre-loaded to check if the testing instruments were running normally. The loading in the elastic phase was applied by force control method and cycled three times to obtain the initial stiffness of ABRB specimen at the loading rate of 0.18 mm/s. 30% of the elastic strength was taken as the control load in the elastic phase, specifically 56.4 kN and 45.12 kN for long specimens and short specimens, respectively. After finishing the pre-loading in the elastic phase, the test specimen was loaded by using displacement control method according to the loading protocols as listed in Table 6.

The loading device was a 2500 kN electro-hydraulic servo MTS. The specimen was connected to the clamp through the inner core end plate and a splint by bolts, as shown in Fig. 9. Since the bottom of the tested specimen was not supposed to move during the test, two LVDTs were placed on both sides of the specimen to measure the longitudinal deformation of the inner core. The load-displacement hysteresis curve of the tested specimen was obtained by comparing the average data from the LVDTs with the data collected from MTS system.

Table 6. Loading protocol parameters.

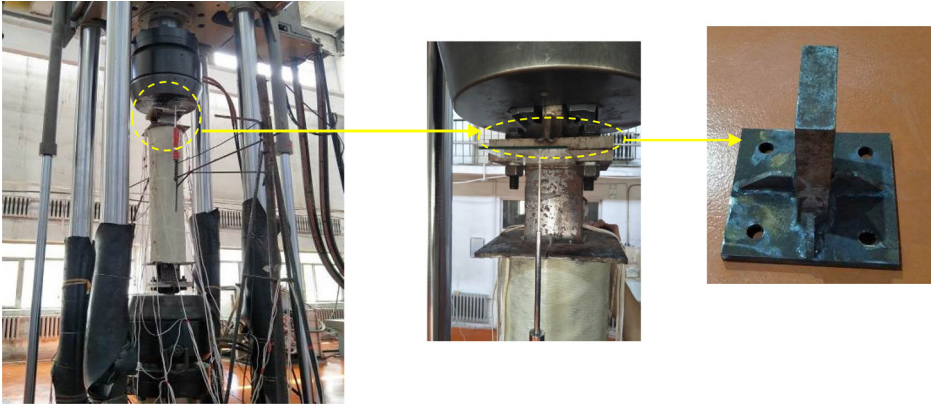|	Inter-story drift ratio	Axial strain	Axial displacement (mm)		Cycling times
			Short specimen	Long specimen	
Loading protocols	2.50‰	1.88‰	1.35	1.68	3
	5.00‰	3.75‰	2.70	3.37	
	7.50‰	5.63‰	4.05	5.06	
	1.00%	7.50‰	5.40	6.75	
	1.25%	9.37‰	6.75	8.44	
	1.50%	1.13%	8.10	10.12	
	1.75%	1.31%	9.45	11.81	
	2.00%	1.50%	10.80	13.50	
	2.40%	1.80%	12.96	16.20	
	2.80%	2.10%	15.12	18.90	
	3.20%	2.40%	17.28	21.60	
	3.60%	2.70%	19.44	24.30	
	4.00%	3.00%	21.60	27.00	

Fig. 9. Connection between specimen and loading device.

5. Test Phenomena

After testing, all the six specimens show similar damage modes. The welding seams between two half-round steel plate were relatively intact, whilst the in-filled concrete did not show obvious cracks. The inner core unit had been fractured in the yielding section, which was close to the transition section between the yielding section and the constrained non-yield section.

Specimen S-B was taken as an example to discuss the test phenomena. Specimen S-B was wrapped with basalt fiber. The deformation was stable when the elastic loading was performed. When loaded to 17.57 mm, the strength of the tested specimen dropped sharply when a sharp sound was heard. Subsequently the inner core fractured and the loading stopped. The breaking position of specimen S-B was at 67 mm from the end of the yielding section as shown in Fig. 10. Cracks appeared on the concrete near the fracture. The multi-wave buckling was obvious near the fracture. The maximum and minimum half-wavelengths of the core unit were 110 mm and 21 mm, respectively. The maximum and minimum wave amplitudes were 71 mm and 5 mm, respectively.

It can be seen from Tables 7 and 8 that the wavenumber and amplitude of the multi-wave buckling of the core units were different. Although there was a large dispersion of the fracture position of the core unit resulting from the gap, material properties, initial defect and friction, the fracture was generally close to the loading end. The half-wavelength near the fracture was shorter and more concentrated. The waveform approximation was similar to a sine wave whose amplitude was relatively large.

The cracks on concrete near the fracture may indicate the most vulnerable point of the inner core. Moreover, the constrained non-yield segment was in an ideal working state and hardly exhibited lateral deformation. Since only the fiber cloth of specimen L-B was cracked during the test, the multi-wave buckling amplitude of

(a) Specimen after test

(b) Core unit

Fig. 10. Test phenomena of specimen S-B.

Table 7. Multi-wave buckling amplitude of core unit.

Number	S-B	S-G	S-C	L-B	L-G	L-C
1	48	129	70	55	12	103
2	27	62	43	83	5	52
3	58	42	46	64	4	22
4	30	32	3	29	20	106
5	47	118	7	130	48	49
6	51	18	76	118	63	86
7	26	6	111	133	53	67
8	26	91	125	220	81	72
9	71	97	116	137	79	74
10	45	92	—	165	18	45
11	51	67	—	—	18	46
12	52	53	—	—	54	28
13	5	—	—	—	18	—
14	20	—	—	—	44	—
15	63	—	—	—	—	—
Amplitude (mm)	71	129	125	220	81	106
Average (mm)	41.3	67.3	66.3	113.4	36.9	62.5

specimen L-B was large. It may result from the fact that the basalt material degradation is poor, and the gap in specimen L-B should be larger. The half-wavelength of the long specimens was larger than that of the short ones. In the test, the long specimen and the short specimen gap control were the same, which was in good agreement with the actual one. The restraint effect of three fiber clothes was good and showed no significant difference.

Table 8. Multi-wave buckling half-wavelength of core unit.

Number	S-B	S-G	S-C	L-B	L-G	L-C
1	40	38	105	51	45	70
2	55	40	121	67	104	54
3	89	59	74	123	69	57
4	101	29	90	100	59	54
5	50	42	29	81	90	51
6	54	31	38	92	104	58
7	47	50	53	48	52	43
8	31	37	106	79	65	54
9	42	83	80	91	28	44
10	50	45	26	88	85	123
11	28	118	34	43	45	126
12	21	57	—	53	46	97
13	24	60	—	—	25	112
14	24	—	—	—	59	—
15	28	—	—	—	25	—
16	24	—	—	—	49	—
17	26	—	—	—	—	—
Max (mm)	101	118	121	123	104	126
Min (mm)	21	29	26	43	25	43
Average (mm)	43.2	53.0	68.7	76.3	59.4	72.5

6. Test Results' Analysis

6.1. *Hysteretic curves*

Figure 11 shows the hysteretic loops of the six specimens. It could be observed that all the specimens show excellent performance in terms of the strength and ductility in the test, namely exhibiting stable hysteretic responses. During the transition from the tension section to the compression section, the obvious "local fluctuation" of hysteretic curves is mainly due to the multiple-wave buckling of core unit plates. When the specimen was unloaded, apparent stiffness degradation is observed. As the multi-wave buckling became clearer, the stiffness degradation tends to be more serious. When the displacement increases, the slope of the curve is reduced when unloading.

6.2. *Ductility analysis*

The cumulative plastic ductility (CPD) is a normalized index to describe the plastic demand on an ABRB,

$$\text{CPD} = \sum_i \frac{|\Delta_{pi}^+ - \Delta_{pi}^-|}{\Delta_y}, \tag{1}$$

where Δ_{pi}^+ and Δ_{pi}^- are, respectively, the maximum positive and negative plastic displacements, during each visit i into the inelastic range.

(a) S-B   (b) S-G   (c) S-C
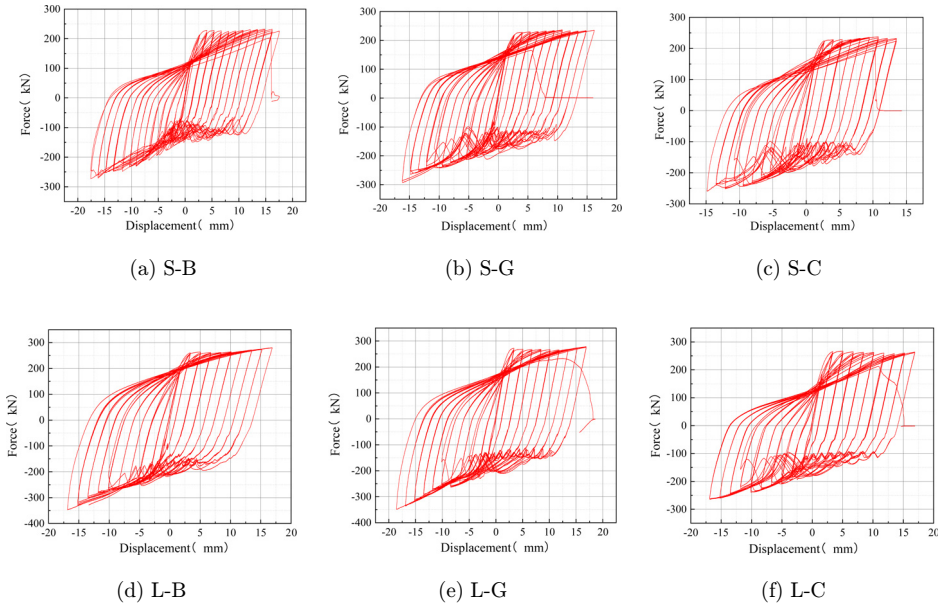
(d) L-B   (e) L-G   (f) L-C

Fig. 11. Hysteretic curves of specimens.

The relationship of CPD and cycle number of the specimens is shown in Fig. 12. Generally, the trend of the CPD curves is similar, indicating that the ductility of the specimens is relatively stable. The CPD increases with the increase of the number of loading cycles. The CPD of all the specimens is greater than 400. The CPD curve of S-B partly deviates from that of S-C/S-G, resulting from the fact that the S-B was welded at the end of the two angles. Consequently, the restraint unit borne the axial load and limited the plasticity development of the core unit.

(a) Short specimens   (b) Long specimens
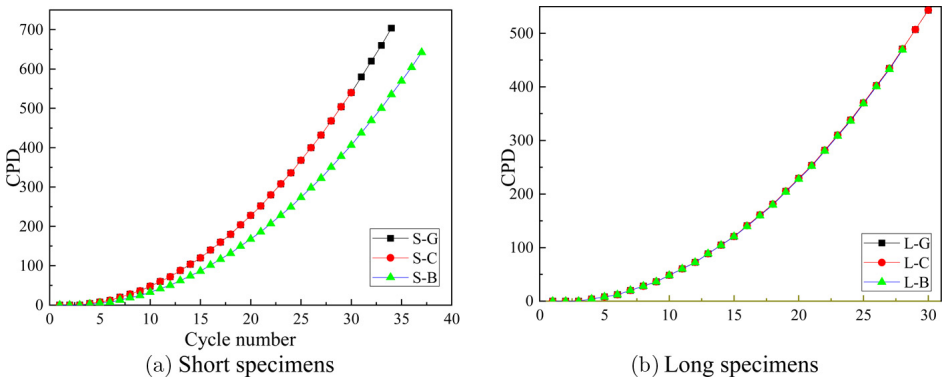
Fig. 12. The relationship of CPD and cycle number.

Table 9. Ductility assessment.

Specimen	S-G	S-C	S-B	L-G	L-C	L-B
Cycle	34	30	37	30	29	28
μ_D	11.01	9.99	12.02	10.05	9.05	9.05
CPD	703.89	539.99	642.16	543.03	543.21	469.06

The displacement ductility ratio μ_D is also introduced to assess the deformation capacity of the specimens, which is defined by

$$\mu_D = \frac{\Delta_m}{\Delta_y},\tag{2}$$

where Δ_y and Δ_m, respectively, are the yielding displacement and the maximum displacement in each loading cycle.

The cumulative plastic ductility (CPD) and displacement ductility ratios of all test specimens are listed in Table 9. The μ_D of S-B reaches 12.02, whilst the μ_D of other specimens are also greater than 9. The comparison shows that the short specimens show better ductility than the long specimen.

6.3. *Energy dissipation capacity*

As an energy consumption component, the energy dissipating ability of ABRB is an important index to evaluate its energy dissipation performance. To assess the energy dissipation ability of the tested specimens, the cumulative energy E_h, secant stiffness K_i, energy dissipation ratio ψ and equivalent viscous damping coefficient h_e are calculated on the basis of tested results as shown in Fig. 13.

The cumulative energy, E_h, is the sum of the area enclosed by force F versus displacement Δ in hysteretic loops, representing the hysteretic energy dissipated by the specimens, as described in Eq. (3). The secant stiffness K_i is directly extracted from the recorded loops and calculated using Eq. (4). The energy dissipation ratio ψ is defined by dividing the dissipated energy by the total work done by the forces, as

(a) Secant stiffness K_i (b) Energy dissipation ratio   (c) Equivalent viscous damping coefficient h_e
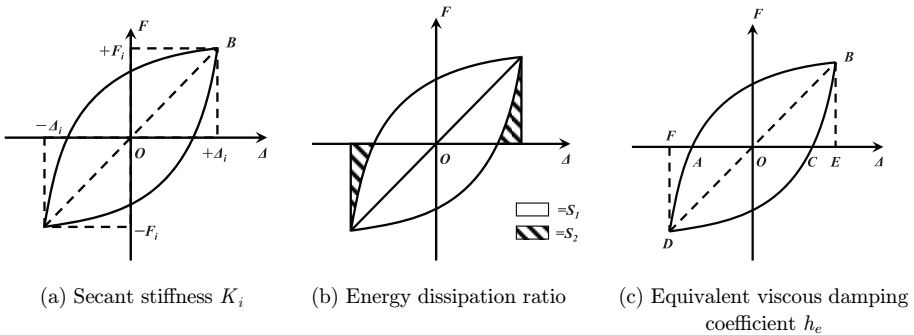
Fig. 13. Definition of energy dissipation indexes.

described by Eq. (5). It is obvious that large ψ implies sufficient energy dissipation capacity. Under cyclic loading conditions, the strength and stiffness of ABRB decrease, which is depicted by the equivalent viscous damping coefficient h_e as described in Eq. (6). The value of h_e represents the ratio of the dissipated energy (areas of ABC and CDA) to the absorbed energy (areas of OBE and ODF) of the equivalent elastic component that undergoes to the same displacement,

$$E_h = \sum_i \int F_i d\Delta, \tag{3}$$

$$K_i = \frac{|+F_i| + |-F_i|}{|+\Delta_i| + |-\Delta_i|}, \tag{4}$$

where K_i is the secant stiffness in the ith recorded loop; F_i and Δ_i are the maximum load and displacement in the ith recorded hysteric loop, respectively,

$$= \frac{S_1}{S_1 + S_2}, \tag{5}$$

$$h_e = \frac{1}{2\pi} \frac{\text{area(ABC + CDA)}}{\text{area(OBE + ODF)}}, \tag{6}$$

where S_1 and S_2 are the absorbed energy and the discharged energy, respectively; and $S_1 + S_2$ gives the total work done by the horizontal force. ABC, CDA, OBE and ODF represent the geometric shapes in Fig. 13(c).

As is shown in Fig. 14, the cumulative energy E_h of specimen S-G is higher than that of S-C and S-B, indicating that its cumulative energy consumption effect is better. The energy consumption area of the tested specimen is steadily increasing, indicating that the energy dissipation performance of the tested specimens is relatively stable.

There is a slight difference in the secant stiffness K_i of the short specimens. It may be due to the influence of the initial defects and the gap in the specimens. The secant stiffness of the specimens decreases with the increase of the axial strain and tends to be consistent at the maximum displacement, degrading to $16\,\text{kN/mm}$.

The energy dissipation ratio ψ of the tested short specimens is more than 90%, indicating that the energy consumption performance of the tested short specimens is good. The energy consumption ratio ψ of the three short specimens is relatively close, indicating that the energy consumption effect is relatively stable.

The equivalent viscous damping coefficient h_e of the short specimens is relatively close at the end, all of which are around 0.33. It indicates that the energy consumption of the test specimen is good. The equivalent damping coefficient of the test specimen S-C and S-G has a certain fluctuation at the axial strain of 1.5%. It may be due to the fact that the multi-wave buckling becomes more obvious. The equivalent viscous damping coefficient h_e of the test specimen is closely related to the hysteresis curve of the tested specimen.

(a) Cumulative energy E_h

(b) Secant stiffness K_i

(c) Energy dissipation ratio

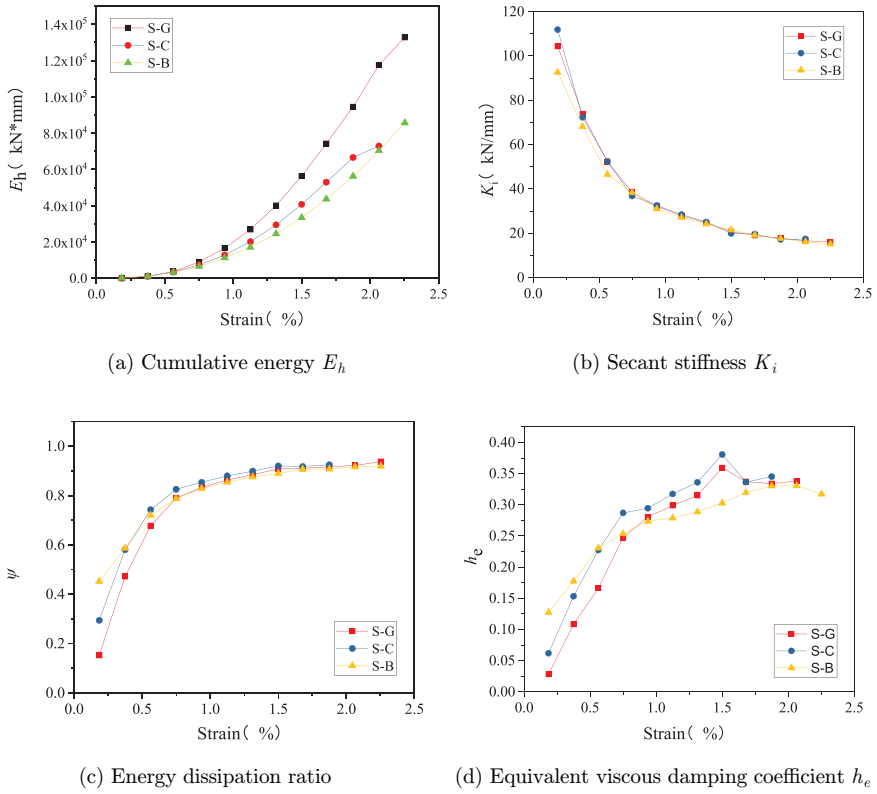
(d) Equivalent viscous damping coefficient h_e

Fig. 14. Energy dissipation capacity of short specimens.

As shown in Fig. 15, the cumulative energy E_h of the long specimens is relatively close to each other. The energy consumption performance of the long specimen is also as stable as that of the short ones. The change trend of the secant stiffness K_i of the long specimens is similar to that of the short specimens. The energy dissipation ratio

(a) Cumulative energy E_h

(b) Secant stiffness K_i
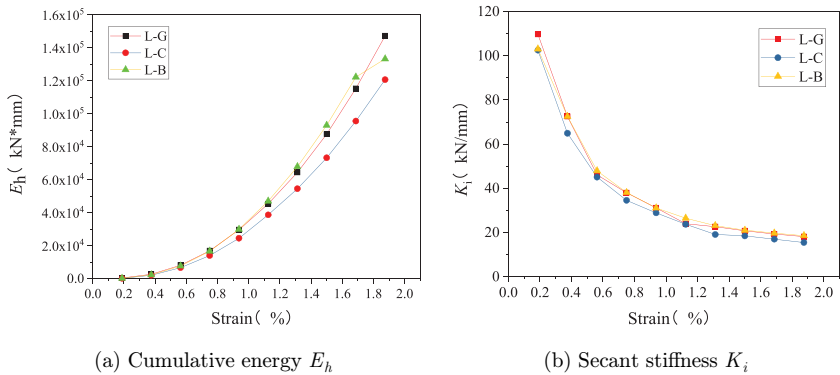
Fig. 15. Energy dissipation capacity of long specimens.

(c) Energy dissipation ratio

(d) Equivalent viscous damping coefficient h_e
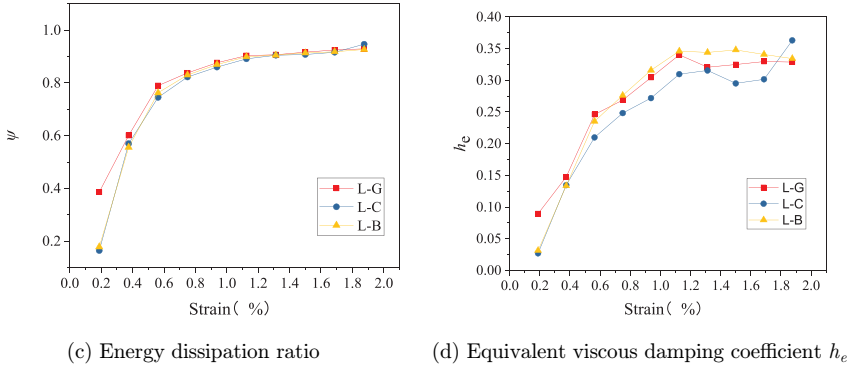
Fig. 15. (*Continued*)

ψ of the long specimens reaches more than 93% and close to each other, indicating that the energy consumption performance of the long specimen is similar to that of the short ones. The change trend of the equivalent viscous damping coefficient h_e of the long specimens also confirms this fact.

7. Finite Element Analysis

7.1. *Model development*

7.1.1. *Elements and interaction*

In the finite element simulation, C3D8R elements are used to simulate core unit and in-filled concrete whilst S4R elements for half-round steel tube and FRP cloth. Surface-to-surface contact is used to simulate the interaction between core unit and in-filled concrete as shown in Fig. 16.

Since no slippage was observed in the interfaces of FRP cloth-steel tube-inner concrete, *Tie command is used to present the interaction property of the interfaces.

(a) Core unit   (b) Infilled concrete   (c) Steel tube   (d) FRP cloth
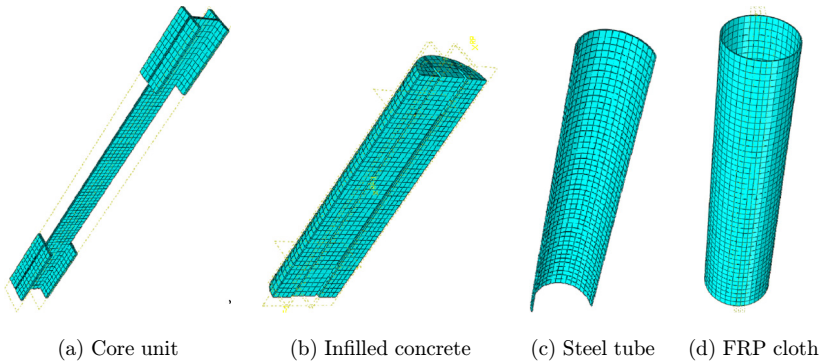
Fig. 16. Finite element model.

7.1.2. *Material modelling*

Based on von Mises yield criterion, bilinear kinematic hardening model is used to present steel properties, as shown in Fig. 17. The bilinear kinematic hardening model was built with the stress–strain relationship of the test material, and the yield stress, ultimate stress, elastic modulus and strain-hardening modulus were determined based on the material characteristic tests. So the bilinear kinematic hardening model can be used to represent the characters of test materials, and the plastic development and damage evolution can be reflected very well in the bilinear kinematic hardening model. The slope in the hardening phase of the curve is 3% of the elastic modulus E_s. Concrete Damaged Plasticity (CDP) model provided in ABAQUS could well present the damage behavior of concrete. To consider the confinement of external tube and FRP cloth to infilled concrete, the constitutive model for confined concrete proposed by Han[19] is introduced into the CDP model as described in Eqs. (7) and (8). To simplify the analysis, linear reduction is used in the descending stage for the concrete under tension.

In compression

$$y = \begin{cases} 2 \cdot x - x^2 & (x \leq 1) \\ \dfrac{x}{\beta_0 \cdot (x-1)^2 + x} & (x > 1) \end{cases}, \tag{7}$$

where

$$x = \frac{\varepsilon}{(1300 + 12.5 \cdot f_c) \cdot 10^{-6} + 800 \cdot (\frac{A_s \cdot f_y}{A_c \cdot f_c})^{0.2} \cdot 10^{-6}},$$

$$y = \frac{\sigma}{f_c},$$

$$\beta_0 = (2.36 \times 10^{-5})^{[0.25+(\frac{A_s \cdot f_y}{A_c \cdot f_{ck}}-0.5)^7]} \mathrm{g}(f_c)^{0.5} \mathrm{g} 0.5.$$

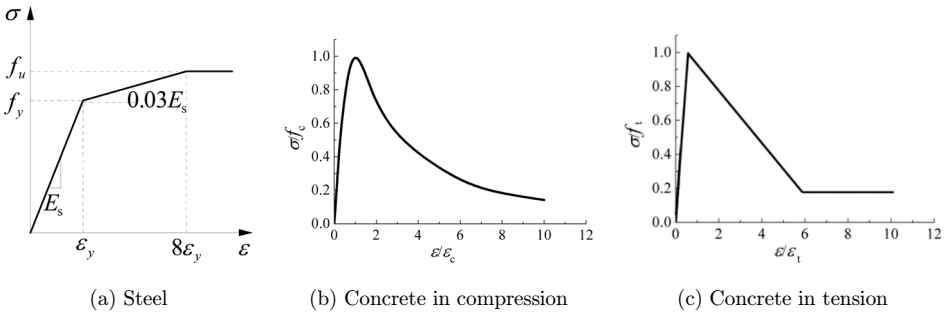(a) Steel   (b) Concrete in compression   (c) Concrete in tension

Fig. 17. Stress–strain relationship of steel and concrete.

In tension

$$y = \begin{cases} 1.2 \cdot x - 0.2 \cdot x^6 & (x \leq 1) \\ \dfrac{x}{0.31 \cdot \sigma_p^2 \cdot (x-1)^{1.7} + x} & (x > 1) \end{cases}, \qquad (8)$$

where

$$x = \frac{\varepsilon}{43.1 \cdot 0.26 \cdot (1.25 \cdot f_c)^{2/3} (\mu \varepsilon)},$$

$$y = \frac{\sigma}{0.26 \cdot (1.25 \cdot f_c)^{2/3}}.$$

Considering the anisotropic properties of FRP cloth, *Lamina property provided by ABAQUS is used. The two-dimensional Hashin's fiber composite damage model[20–22] is adopted for presenting the damage criterion of FRP cloth, including fiber tension, fiber compression, matrix tension and matrix compression, as follows. The tested properties of three fibers in Table 5 are introduced into the material model.

Fiber in tension

$$(\hat{\sigma}_{11} \geq 0) \quad F_f^t = \left(\frac{\hat{\sigma}_{11}}{X^T}\right)^2 + \alpha\left(\frac{\hat{\tau}_{12}}{s^L}\right)^2 \geq 1, \qquad (9)$$

Fiber in compression

$$(\hat{\sigma}_{11} \leq 0) \quad F_f^c = \left(\frac{\hat{\sigma}_{11}}{X^C}\right)^2 \geq 1, \qquad (10)$$

Matrix in tension

$$(\hat{\sigma}_{22} \geq 0) \quad F_m^t = \left(\frac{\hat{\sigma}_{22}}{Y^T}\right)^2 + \left(\frac{\hat{\tau}_{12}}{s^L}\right)^2 \geq 1, \qquad (11)$$

Matrix in compression

$$(\hat{\sigma}_{22} \leq 0) \quad F_m^c = \left(\frac{\hat{\sigma}_{22}}{2S^T}\right)^2 + \left[\left(\frac{Y^C}{2S^T}\right)^2 - 1\right]\frac{\hat{\sigma}_{22}}{Y^C} + \left(\frac{\hat{\tau}_{12}}{S^L}\right)^2 \geq 1, \qquad (12)$$

where X^T and X^C are the longitudinal tensile and compressive strength, respectively; Y^T and Y^C are the transverse tensile and compressive strength, respectively; S^L and S^T are the longitudinal and transverse shear strength, respectively; α is the factor related to the effect of the shear stress on the tensile initiation criterion of fiber; $\hat{\sigma}_{11}$, $\hat{\sigma}_{22}$ and $\hat{\tau}_{12}$ are the in-plane effective longitudinal, transverse and shear stress tensor components of FRP, respectively.

7.1.3. *Initial imperfection modeling*

The real initial imperfection distributing in the core unit is kind of hard to precisely present in the model. In that case, to simplify the modeling, the first-order buckling mode is taken as the initial imperfection as shown in Fig. 18. 1/1000 of the core unit span is introduced as the maximum deflection at mid-span.

7.2. *Model validation and result analysis*

The finite element models are developed for the six specimens by using ABAQUS. As shown in Fig. 19, the deviation between the bearing capacity of the finite element simulation and the test is small. Some specific factors may result in the difference in these curves. For instance, the hysteretic curves of specimen L-C and the corresponding model are generally in good agreement, but there is some difference on the tension side. During the test, the bearing capacity of the specimen was attenuated at the later stage, which may be due to the damage caused by the overall buckling of the core unit in the previous period. The skeleton curves of the test specimen based on these hysteretic curves are also shown in Fig. 19, and it can be seen that the difference in the bearing capacity between the specimens and the models is within about 5%.

The out-plane buckling deformation and crack positions of the core unit in test specimens is illustrated in Fig. 20(a), which are displayed as 20 times of actual deformations, the same as the simulated results as shown in Fig. 20(b). When the buckling mode transferred from low-order modal to high-order modal, the length of the middle horizontal segment is $kl_i = 2\pi$, and the moment of which is zero.

The simulation caught the multi-wave buckling very well, and clear local deformation occurred in the inner core of ABRB. From the comparison of test phenomena and simulation results, the multi-wave buckling deformation modes are almost same between experiment and simulation. There are some differences in qualitative buckling deformation amplitudes. As shown in Table 10, the tested and simulated wave lengths of multi-wave buckling are in good agreement whose differences are between 1.31% and 26.7%.

In general, the results of the finite element analysis are close to the test results, which can reflect the force mechanism and energy consumption of the specimens; the geometric deformation states of the finite element models during the simulation are also consistent with the tested results. The final failure of ABRBs was due to the fatigue fracture of inner cores, which was directly related to the cyclic buckling deformation of inner cores as a multi-wave mode. The material cracking is simulated

Fig. 18. Initial imperfection modeling.

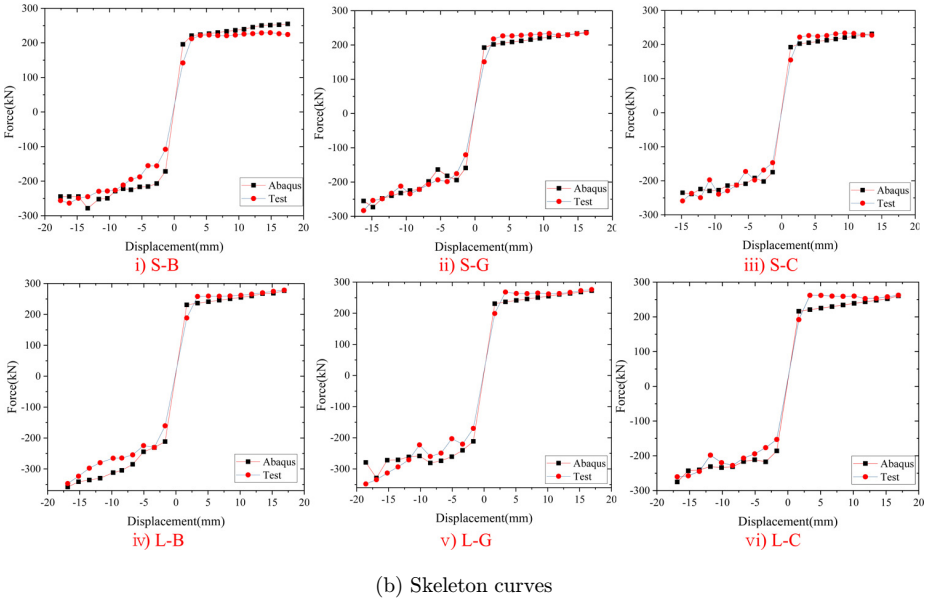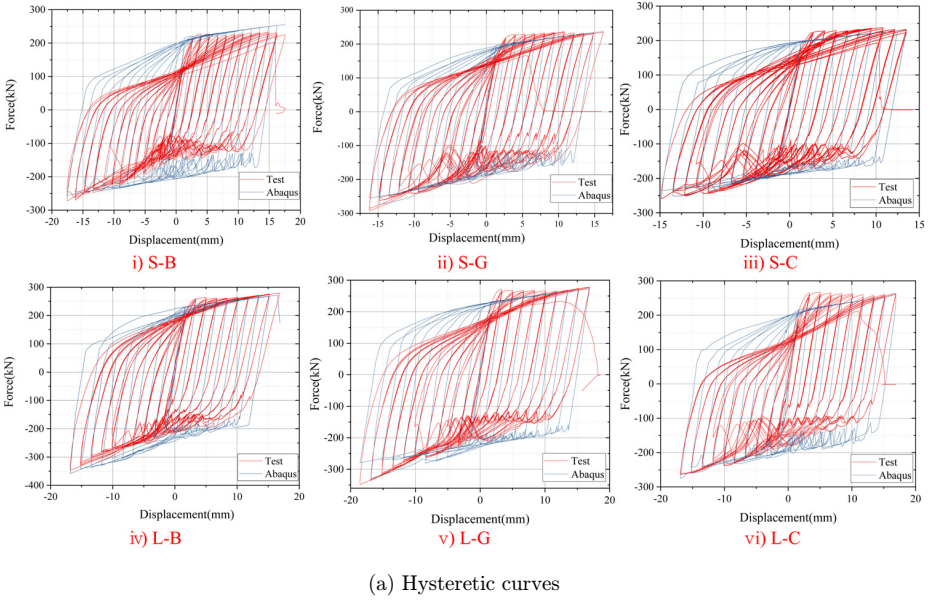(a) Hysteretic curves

(b) Skeleton curves

Fig. 19. Model validation.

with strength decreasing, and there is a little gap that existed between test and simulation. The manufacturing operation also affects the global and local behavior of ABRB, which cannot be simulated absolutely in the finite element model. It can be seen that the simulated hysteretic curves can reflect the most obvious overall
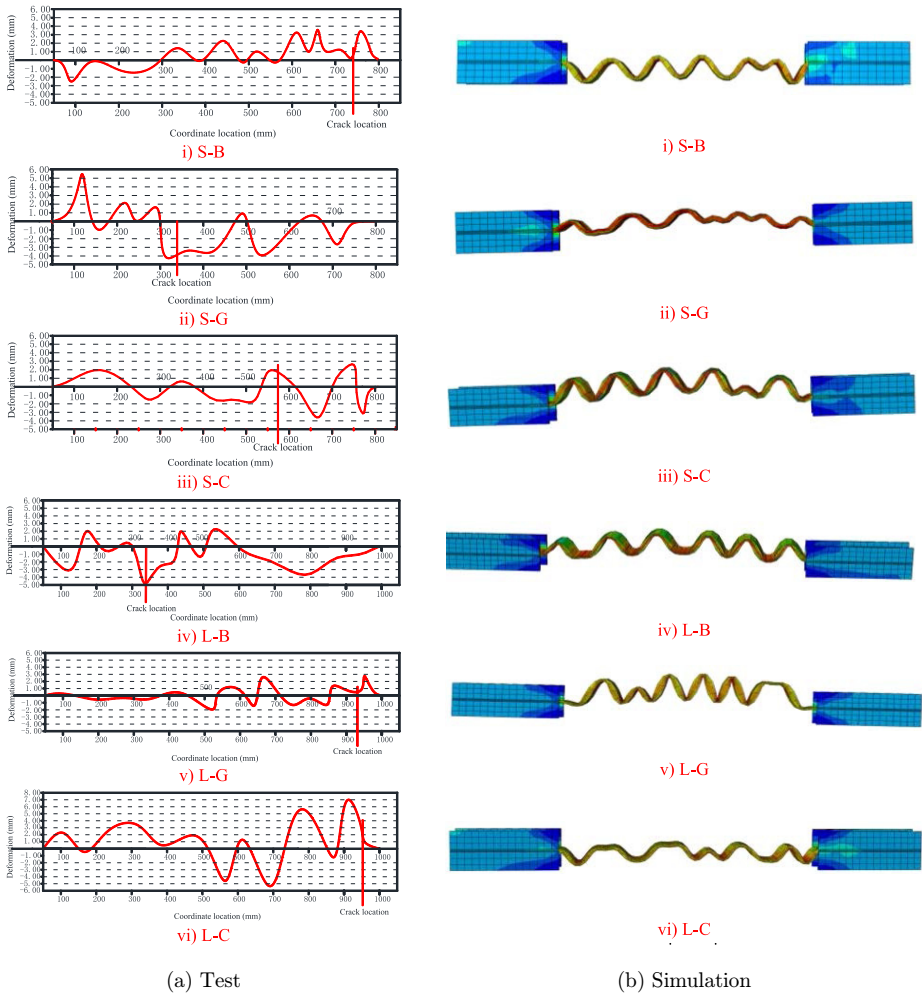
(a) Test   (b) Simulation

Fig. 20. Overall buckling deformation (enlarged by 20 times).

buckling phenomena of the specimens, but the simulation for the stiffness degradation of the specimen after the overall buckling during the test can only be demonstrated to a certain extent.

As shown in Fig. 21 and Table 11, the stress of carbon fiber is bigger than those of basalt fiber and glass fiber under lateral thrust when local buckling occurred.

Table 10. Comparison of tested and simulated wave lengths.

Specimens	S-B	S-C	S-G	L-B	L-C	L-G
Experimental wave lengths l_e (mm)	86	136	106	152	145	118
Simulation wave lengths l_s (mm)	109	120	103	150	148	138

(a) Short specimens

(b) Long specimens
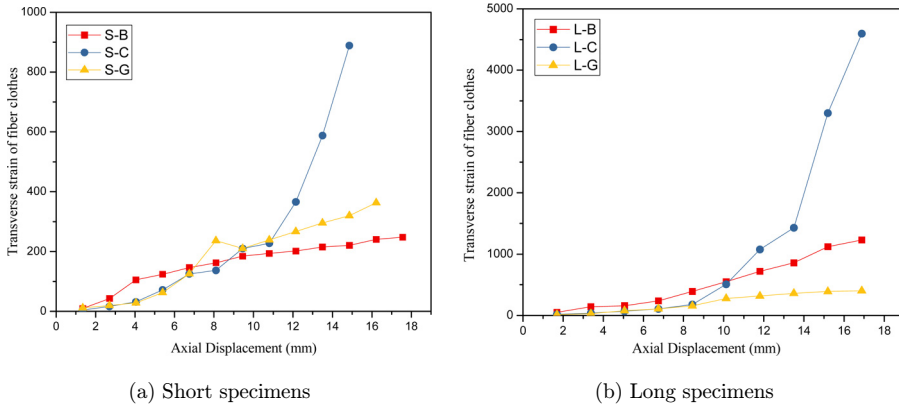
Fig. 21. Transverse strain of the fiber clothes in specimens.

Table 11. Stress verification of FRP in specimens.

Specimens	S-B	S-C	S-G	L-B	L-C	L-G
Maximum load P (kN)	270	255	290	340	270	350
Fiber strength (MPa)	94	725	250	94	725	250
Fiber stress (MPa)	87.5	117	151	111	105	176

The flexural rigidity of concrete filled steel tubes is very large; therefore, no visible deformations were observed in the concrete filled steel tubes. The lateral thrust of inner cores is resisted by the outer wrapped fiber clothes. The stress contours of the outer wrapped fiber clothes under maximum load are shown in Fig. 22, which are compared to the results in Table 11.

Carbon fiber has high strength and good performance. However, the performance of the ABRB wrapped by carbon fiber is lower than that of glass fiber, indicating that the FRP restraining effect is not only related to the material properties of FRP, but also the specific member configuration. In the test, the strength of basalt fiber is the smallest, and only the basalt fiber of specimen L-B was fractured. According to the stress contours of basalt fiber in Fig. 22, the maximum stress of basalt fiber is 132 MPa, which is larger than the strength of basalt fiber; therefore, the fiber fractured at the end of outer restraint in L-B which is in consistency with the test, indicating that the simulated results agreed with the experimental phenomena.

7.3. *Parametric analysis*

The model with CFRP is used as the control model, since CFRP fiber exhibits the best performance in the three kinds of fibers. The gap between core unit and concrete, friction between core unit and concrete, and CFRP thickness are considered as main parameters in the following simulation.
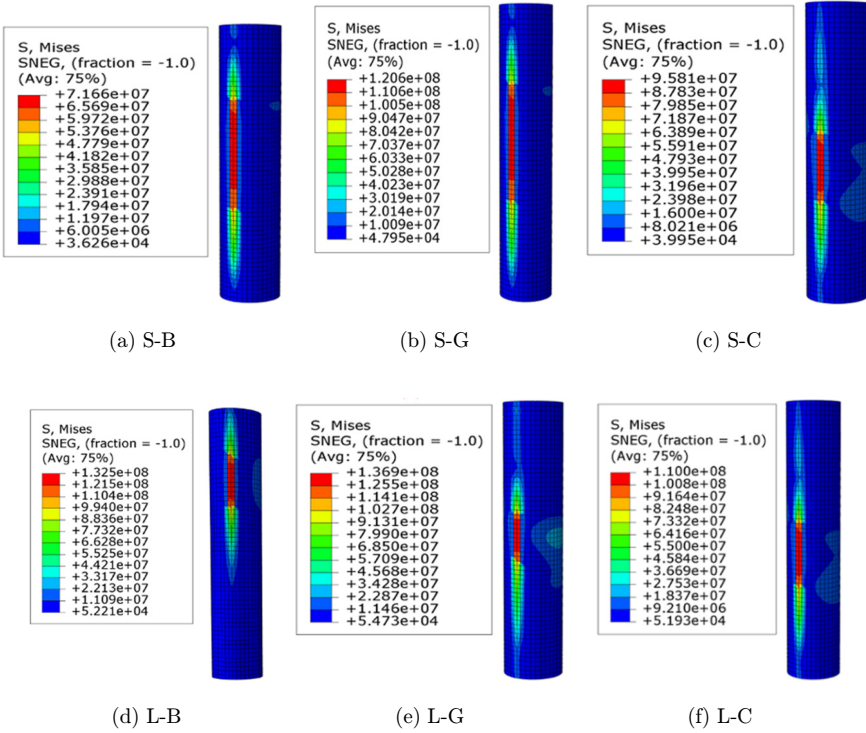
(a) S-B   (b) S-G   (c) S-C

(d) L-B   (e) L-G   (f) L-C

Fig. 22. Maximum stress of fiber clothes.

7.3.1. *Influence of gap between core unit and concrete*

The gaps between inner core unit and infilled concrete in the models are 0.5 mm, 1 mm, 2 mm and 3 mm, respectively, and the hysteretic curves and energy dissipation indexes are shown in Figs. 23 and 24.

    With the increase of the gap between inner core and infilled concrete, the pinch and fluctuation of hysteretic curves become more obvious, especially for the compression parts of the curves, as the calculation running of the model also becomes more difficult. When the gap is larger than 3 mm, the calculation convergence cannot be achieved in the model. The phenomena result from the fact that increasing the gap would cause more obvious local buckling of core unit. With the local buckling development in core unit, constraint members would sustain more lateral force which further increases the gap and aggravates the local buckling of core unit. On the contrary, over-small gap would cause Poisson effect, as shown in Fig. 24(a), namely the lateral deformation of core unit directly resulting from its vertical deformation under certain Poisson's ratio. The gap between inner core and infilled concrete shows slight effects on secant stiffness and energy dissipation ratio, but negatively correlated to equivalent viscous damping coefficient, which is directly related to the energy dissipation factor.
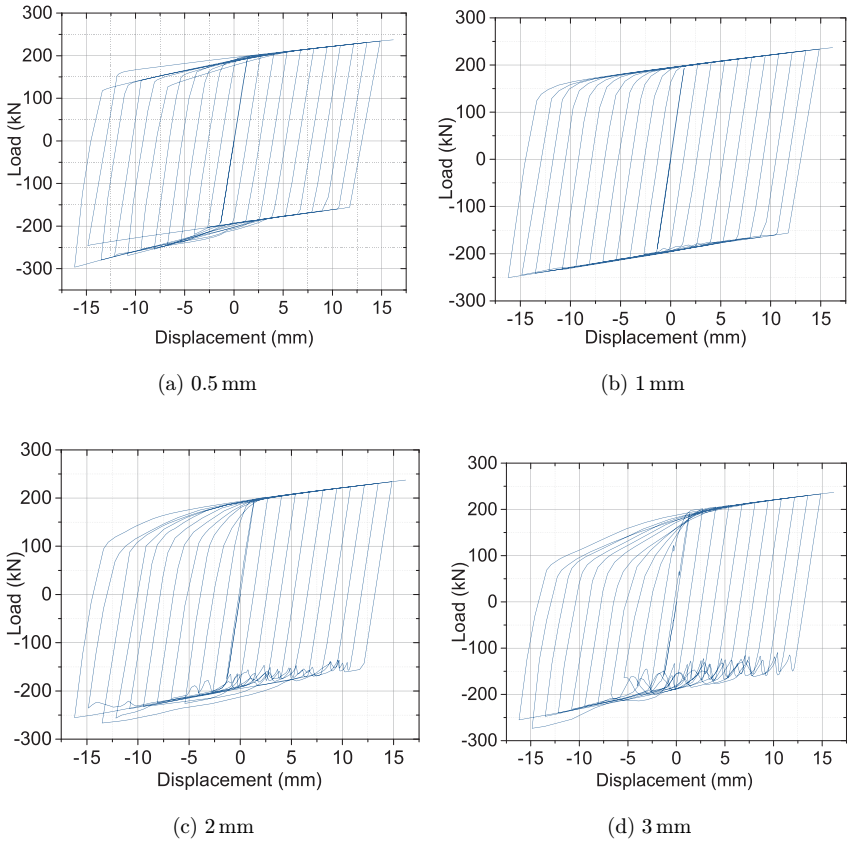
(a) 0.5 mm

(b) 1 mm

(c) 2 mm

(d) 3 mm

Fig. 23. Influence of gap on hysteretic curves.

(a) Secant stiffness K_i
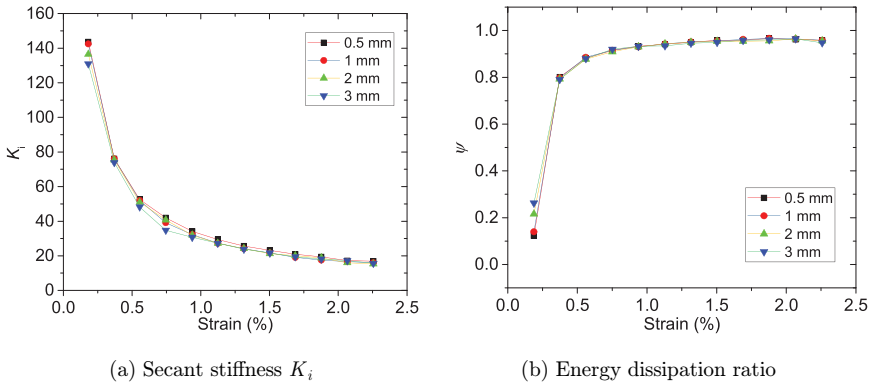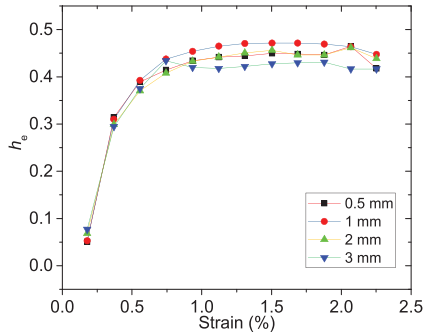
(b) Energy dissipation ratio

Fig. 24. Influence of gap on energy dissipation capacity.

(c) Equivalent viscous damping coefficient h_e

Fig. 24. (*Continued*)

7.3.2. *Influence of friction between core unit and concrete*

The friction factors between inner core unit and infilled concrete in the models are 0 (namely, no friction), 0.1, 0.2 and 0.3, respectively. The corresponding hysteretic curves and energy dissipation indexes are shown in Figs. 25 and 26.

With the increase of friction factor, the hysteretic performance of the model is improved, especially for the compression parts of the curves, whilst the stress level of the core unit is increased. The fluctuation of the curves results from the contact between the multi-wave buckled core unit and infilled concrete under compression. The increase of friction force would also cause the deformation concentration of the core unit and then change the failure mode of the model. Friction factor shows subtle effect on the energy dissipation indexes of the models. The negative correlation between friction factor and equivalent viscous damping coefficient results from the increase of axial force in core unite with large friction factor causing the reduction of energy dissipation effect.
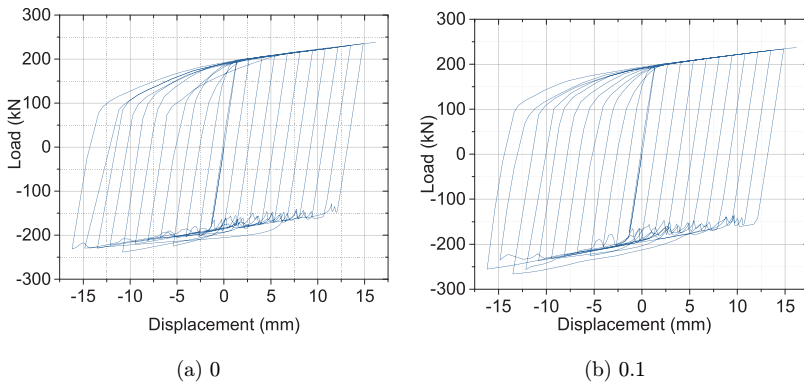

(a) 0

(b) 0.1

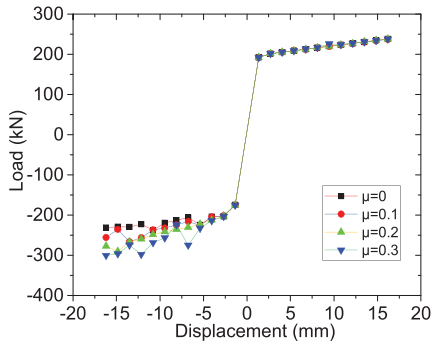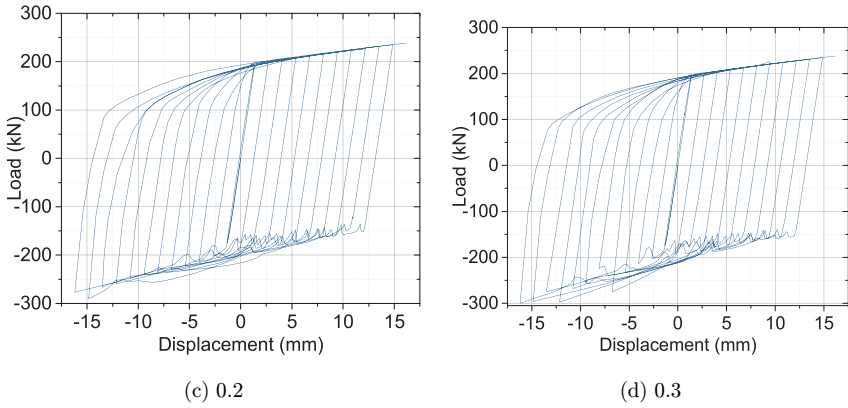Fig. 25. Influence of friction factor on hysteretic curves.

(c) 0.2

(d) 0.3

(e) skeleton curves

Fig. 25. (*Continued*)
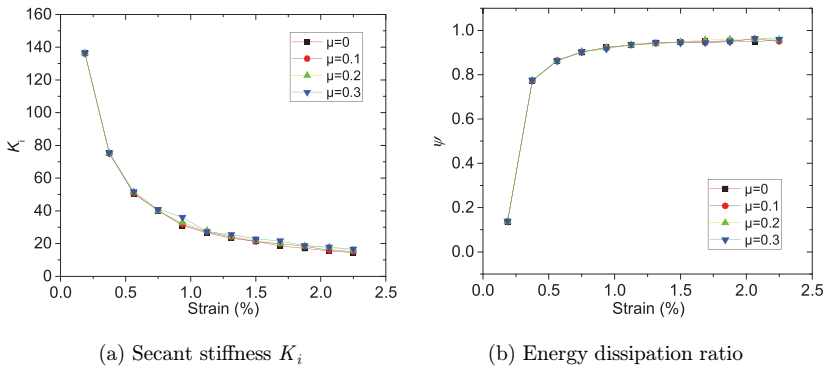

(a) Secant stiffness K_i
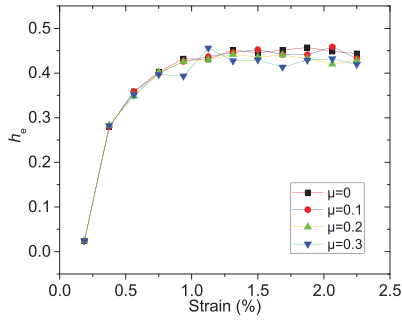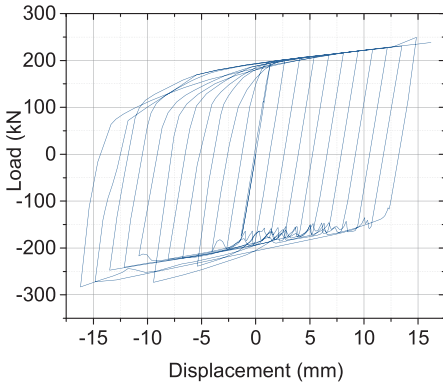

(b) Energy dissipation ratio

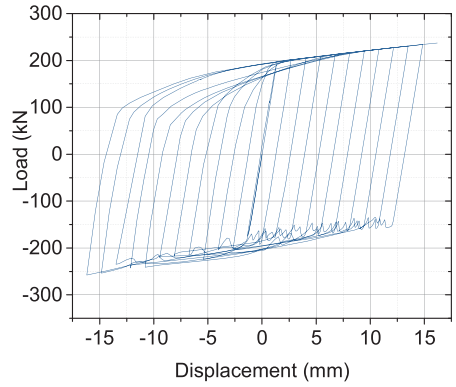Fig. 26. Influence of friction factor on energy dissipation capacity.
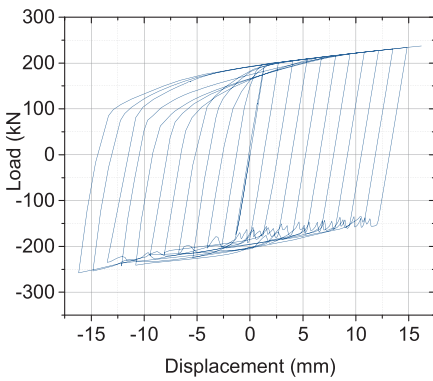
(c) Equivalent viscous damping coefficient h_e

Fig. 26. (*Continued*)

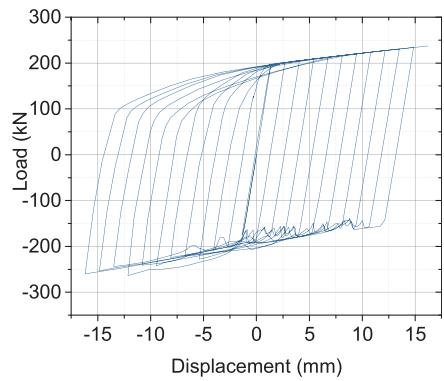(a) 1 mm

(b) 2 mm

(c) 3 mm

(d) 4 mm

Fig. 27. Influence of FRP thickness on hysteretic curves.

(a) Secant stiffness K_i

(b) Energy dissipation ratio

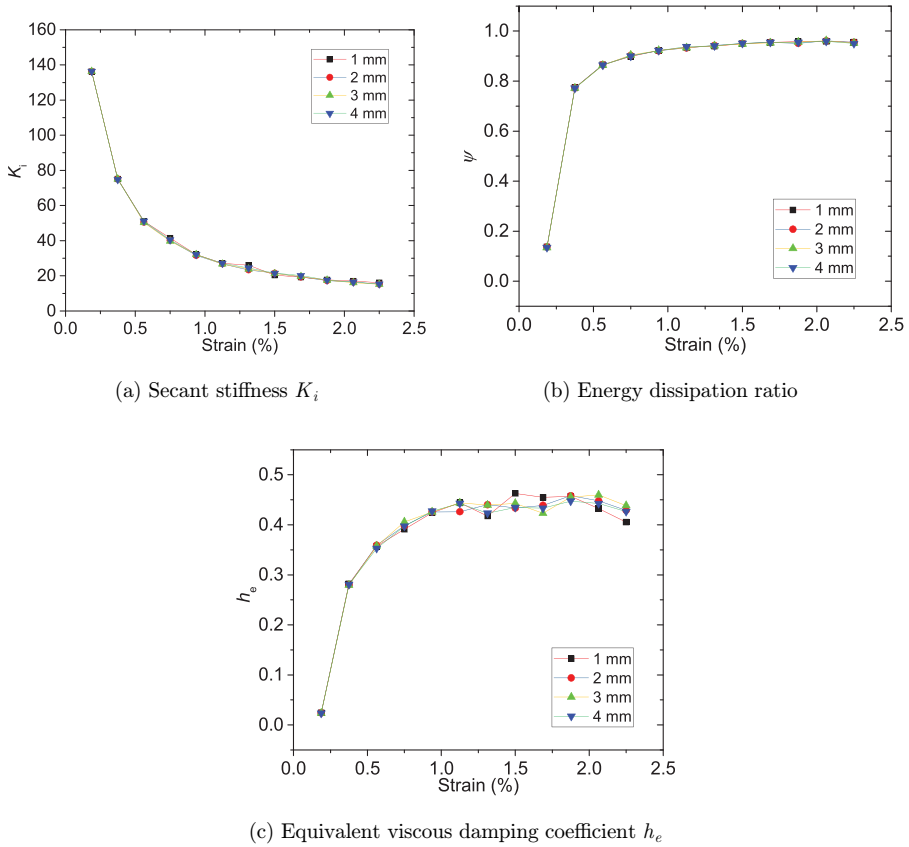(c) Equivalent viscous damping coefficient h_e

Fig. 28. Influence of FRP thickness on energy dissipation capacity.

7.3.3. *Influence of FRP thickness*

The thicknesses of the FRP cloth confining the ABRB in the models are 1 mm, 2 mm, 3 mm and 4 mm, respectively. The corresponding hysteretic curves and energy dissipation indexes are shown in Figs. 27 and 28. With the increase of FRP thickness, the hysteretic curves of the models become plumper, especially from 1 mm to 2 mm, as the fluctuation of the curves is also attenuated. The thickness of FRP cloth shows little influence on the energy dissipation capacity of the models, except for the little fluctuation on the equivalent viscous damping coefficient. Since the basalt fiber fractured in the test, the design of FRP cloth is still necessary. Over-thin FRP cloth with low strength would also affect the hysteretic behavior of ABRB.

8. Conclusions

In this paper, a series of cyclic tests on six ABRBs wrapped with three kinds of FRPs (carbon fiber, glass fiber and basalt fiber) were performed. Based on a finite element

model validated against the test result, a parametric analysis is performed. The main conclusions are drawn as follows:

(1) All the six specimens show similar damage modes. As the in-filled concrete did not show obvious cracks, the inner core unit fractured in the yielding section. The restraint effect of three fiber cloth was good and showed no significant difference, except for the cracked basalt fiber in specimen L-B.

(2) All the specimens show excellent and stable performance in terms of the strength, ductility and energy dissipation ability, except for the local fluctuation in the hysteretic curves due to the multiple-wave buckling of core unit. Short specimens show better ductility but worse energy dissipation ability than the long specimen.

(3) The buckling mode and hysteretic performance of the specimens could be simulated well by the finite element models. Increasing the gap between inner core and infilled concrete would make the pinch and fluctuation of hysteretic curves become more obvious, especially for the compression parts of the curves. With the increase of friction factor, the hysteretic performance of the model is improved, especially for the compression parts of the curves.

(4) Even though the hysteretic curves of the models become plumper, increasing FRP thickness shows subtle effect on the strength and energy dissipation ability of the models. Based on the failure modes in test and the stress contour in simulation, CFRP with large strength is still suggested to be used in the wrapped buckling-restrained brace.

References

1. M. Wakabayashi, T. Nakamura, A. Kashibara *et al.*, Experimental study of elasto-plastic properties of precast concrete wall panels with built-in insulating braces, Summaries of Technical Papers of Annual Meeting, Architectural Institute of Japan (1973), 104121044: 12–20.
2. H. Nakamura, Y. Maeda and T. Takeuchi *et al.*, Fatigue properties of practical-scale unbounded braces, Nippon steel technical report No. 822000.
3. S. Merritt, C. M. Uang ans G. Benzoni, Subassemblage, Testing of Core Brace Buckling-restrained Braces. Report No.TR-2003/01, University of California, San Diego, 2003: 1–120.
4. Deng Kailai and Pan Peng, Study of GFRP steel buckling restraint-braces, *J. Composites Construct. (ASCE)* **19**(6) (2015) 04015009-1-8.

5. M. Iwata and M. Murai, Buckling-restrained brace using steel mortar planks; performance evaluation as a hysteretic damper. *Earthquake Eng. Struct. Dyn.* **35**(14) (2006) 1807–1826.
6. A. Gheidi, M. Mirtaheri, A. P. Zandi *et al.*, Effect of filler material on local and global behaviour of buckling-restrained braces. *Struct. Design Tall Special Build.* **20**(6) (2011) 700–710.
7. C. C. Chou and S. Y. Chen, Subassemblage tests and finite element analyses of sandwiched buckling-restrained braces. *Eng. Struct.* **32**(8) (2010) 2108–2121.
8. T. Takeuchi, J. F. Hajjar, R. Matsui *et al.*, Effect of local buckling core plate restraint in buckling restrained braces. *Eng. Struct.* **44** (2012) 304–311.
9. Eryasar Mehmet Emrah and Topkaya Cem. An experimental study on steel-encased buckling-restrained brace hysteretic dampers, *Earthquake Eng. Struct. Dyn.* **39** (2010) 561–581.
10. M. E. Eryaşar and C. Topkaya, An experimental study on steel-encased buckling-restrained brace hysteretic dampers, *Earthquake Eng. Struct. Dyn.* **39**(5) (2010) 561–581.
11. N. Hoveidae and B. Rafezy, Overall buckling behavior of all-steel buckling restrained braces, *J. Construct. Steel Res.* **79** (2012) 151–158.
12. Gennaa Francesco and Gelfib Piero. Analysis of the lateral thrust in bolted steel buckling-restrained braces, Part1: Experimental and numerical results, *J. Struct. Eng. (ASCE)* **138**(10) (2012) 1231–1243.
13. P. Dusicka and B. Wiley, Concept of buckling restraint of steel braces with fiber reinforced polymers//Proceedings of the 2008 Structures Congress, 2008.
14. C. L. Wang, T. Usami and J. Funayama, Evaluating the influence of stoppers on the low-cycle fatigue properties of high-performance buckling-restrained braces, *Eng. Struct.* **41** (2012) 167–176.
15. C. L. Wang, T. Usami, J. Funayama *et al.*, Low-cycle fatigue testing of extruded aluminum alloy buckling-restrained braces, *Eng. Struct.* **46** (2013) 294–301.
16. D. J. Miller, L. A. Fahnestock and M. R. Eatherton, Development and experimental validation of a nickel–titanium shape memory alloy self-centering buckling-restrained brace, *Eng. Struct.* **40** (2012) 288–298.
17. Jia Mingming, Lu Dagang, Zhang Sumei and Sun Lin, Performance testing and cyclic behavior of buckling-restrained braces with H cross section unrestrained segments, *Adv. Struct. Eng.* **17**(5) (2014) 677–692.
18. Jia Mingming, Guo Lanhui and Lu Dagang. Performance testing and comparison of buckling-restrained braces with H and crisscross cross section unrestrained segments, *Int. J. Steel Struct.* **14**(4) (2014) 745–753.
19. Han Lin-hai, *Concrete-Filled Steel Tubular Structures: Theory & Application* (Beijing, Science Press, 2004).
20. Z. Hashin and A. Rotem, A fatigue failure criterion for fiber reinforced materials, *J. Compos Mater.* **7**(4) (1973) 448–64.
21. Z. Hashin, Failure criteria for unidirectional fiber composites. *J. Appl Mech.* **47**(2) (1980) 329–34.
22. M. Kathiresan, K. Manisekar and V. Manikandan, Crashworthiness analysis of glass fibre/epoxy laminated thin walled composite conical frusta under axial compression, *Composite Struct.* **108** (2014) 584–599.